Proc. *7th International Conference on Medical Image Computing and Computer Assisted Intervention (MICCAI'04)*, Saint Malo, France, 26th-30th September 2004,
In *Lecture Notes in Computer Science*,
Springer Verlag Berlin Heidelberg 2004, in press

A New 3D Parametric Intensity Model for Accurate Segmentation and Quantification of Human Vessels

Stefan Wörz, Karl Rohr

School of Information Technology, Computer Vision & Graphics Group
International University in Germany, 76646 Bruchsal
Email: {woerz,rohr}@i-u.de

Abstract. We introduce an approach for 3D segmentation and quantification of vessels. The approach is based on a new 3D cylindrical parametric intensity model, which is directly fit to the image intensities through an incremental process based on a Kalman filter. The model has been successfully applied to segment vessels from 3D MRA images. Our experiments show that the model yields superior results in estimating the vessel radius compared to approaches based on a Gaussian model. Also, we point out general limitations in estimating the radius of thin vessels.

1 Introduction

Heart and vascular diseases are one of the main causes for the death of women and men in modern society. An abnormal narrowing of arteries (stenosis) caused by atherosclerosis is one of the main reasons for these diseases as the essential blood flow is hindered. Especially, the blocking of a coronary artery can lead to a heart attack. In clinical practice, images of the human vascular system are acquired using different imaging modalities, for example, ultrasound, magnetic resonance angiography (MRA), X-ray angiography, or ultra-fast CT. Segmentation and quantification of vessels (e.g., estimation of the radius) from these images is crucial for diagnosis, treatment, and surgical planning.

The segmentation of vessels from 3D medical images, however, is difficult and challenging. The main reasons are: 1) the thickness (radius) of vessels depends on the type of vessel (e.g., relatively small for coronary arteries and large for the aorta), 2) the thickness typically varies along the vessel, 3) the images are noisy and partially the boundaries between the vessels and surrounding tissues are difficult to recognize, and 4) in comparison to planar structures depicted in 2D images, the segmentation of curved 3D structures from 3D images is much more difficult. Previous work on vessel segmentation from 3D image data can be divided into two main classes of approaches, one based on differential measures (e.g., Koller *et al.* [6], Krissian *et al.* [7], Bullitt *et al.* [2]) and the other based on deformable models (e.g., Rueckert *et al.* [10], Noordmans and Smeulders [8], Frangi *et al.* [3], Gong *et al.* [5]). For a model-based 2D approach for measuring intrathoracic airways see Reinhardt *et al.* [9]. The main disadvantage of differential measures is that only local image information is taken into account, and

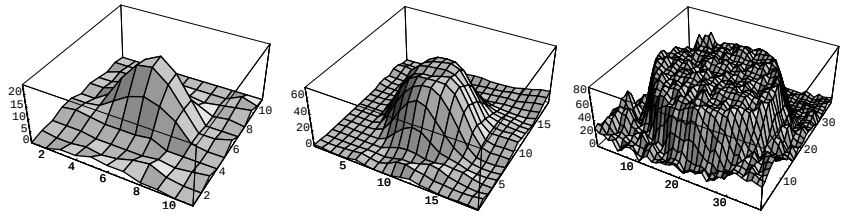

Fig. 1. Intensity plots of 2D slices of a thin vessel in the pelvis (left), the artery iliaca communis of the pelvis (middle), and the aorta (right) in 3D MR images.

therefore these approaches are relatively sensitive to noise. On the other hand, approaches based on deformable models generally exploit contour information of the anatomical structures, often sections through vessel structures, i.e. circles or ellipses. While these approaches include more global information in comparison to differential approaches, only 2D or 3D contours are taken into account.

We have developed a new 3D parametric intensity model for the segmentation of vessels from 3D image data. This analytic model represents a cylindrical structure of variable radius and directly describes the image intensities of vessels and the surrounding tissue. In comparison to previous contour-based deformable models much more image information is taken into account which improves the robustness and accuracy of the segmentation result. In comparison to previously proposed Gaussian shaped models (e.g., [8],[5]), the new model represents a Gaussian smoothed cylinder and yields superior results for vessels of small, medium, and large sizes. Moreover, the new model has a well defined radius. In contrast, for Gaussian shaped models the radius is often heuristically defined, e.g., using the inflection point of the Gaussian function. We report experiments of successfully applying the new model to segment vessels from 3D MRA images.

2 3D Parametric Intensity Model for Tubular Structures

2.1 Analytic Description of the Intensity Structure

The intensities of vessels are often modeled by a 2D Gaussian function for a 2D cross-section or by a 3D Gaussian line (i.e. a 2D Gaussian swept along the third dimension) for a 3D volume (e.g., [8],[7],[5]). However, the intensity profile of 2D cross-sections of medium and large vessels is plateau-like (see Fig. 1), which cannot be well modeled with a 2D Gaussian function. Therefore, to more accurately model vessels of small, medium, and large sizes, we propose to use a Gaussian smoothed 3D cylinder, specified by the radius R (thickness) of the vessel segment and Gaussian smoothing σ. A 2D cross-section of this Gaussian smoothed 3D cylinder is defined as

$$g_{Disk}\left(x,y,R,\sigma\right) = \mathrm{Disk}\left(x,y,R\right) \ * \ G_{\sigma}^{2D}(x,y) \tag{1}$$

where $*$ denotes the 2D convolution, $\mathrm{Disk}\left(x,y,R\right)$ is a two-valued function with value 1 if $r \leq R$ and 0 otherwise (for $r = \sqrt{x^2+y^2}$), as well as the 2D Gaussian function $G_{\sigma}^{2D}(x,y) = G_{\sigma}\left(x\right) \ G_{\sigma}\left(y\right)$, where $G_{\sigma}\left(x\right) = \left(\sqrt{2\pi}\sigma\right)^{-1} e^{-\frac{x^2}{2\sigma^2}}$. By

exploiting the symmetries of the disk and the 2D Gaussian function as well as the separability of the 2D convolution, we can rewrite (1) as

$$g_{Disk}(x, y, R, \sigma) = 2 \int_{-R}^{R} G_\sigma(r - \eta)\ \Phi_\sigma\left(\sqrt{R^2 - \eta^2}\right)\ d\eta - \left(\Phi_\sigma(r + R) - \Phi_\sigma(r - R)\right) \tag{2}$$

using the Gaussian error function $\Phi(x) = \int_{-\infty}^{x} (2\pi)^{-1/2}\ e^{-\xi^2/2}\, d\xi$ and $\Phi_\sigma(x) = \Phi(x/\sigma)$. Unfortunately, a closed form of the integral in (2) is not known. Therefore, the exact solution of a Gaussian smoothed cylinder cannot be expressed analytically and thus is computationally expensive. Fortunately, in [1] two approximations $g_{Disk<}$ and $g_{Disk>}$ of g_{Disk} are given for the cases $R/\sigma < T_\Phi$ and $R/\sigma > T_\Phi$, respectively (using a threshold of $T_\Phi = 1$ to switch between the cases). Note that the two approximations are generally not continuous at the threshold value T_Φ. However, for our model fitting approach a continuous and smooth model function is required (see Sect. 3 for details). Therefore, based on these two approximations, we have developed a combined model using a Gaussian error function as a blending function such that for all ratios R/σ always the approximation with the lower approximation error is used. The blending function has two fixed parameters for controlling the blending effect, i.e. a threshold T_Φ which determines the ratio R/σ where the approximations are switched and a standard deviation σ_Φ which controls the smoothness of switching. We determined optimal values for both blending parameters (see Sect. 2.2 for details). The 3D cylindrical model can then be written as (using $\mathbf{x} = (x, y, z)^T$)

$$g_{Cylinder}(\mathbf{x}, R, \sigma) = g_{Disk<}(r, R, \sigma)\ \left(1 - \Phi_{\sigma_\Phi}\left(\frac{R}{\sigma} - T_\Phi\right)\right) + g_{Disk>}(r, R, \sigma)\ \Phi_{\sigma_\Phi}\left(\frac{R}{\sigma} - T_\Phi\right) \tag{3}$$

where

$$g_{Disk<}(r, R, \sigma) = \frac{2R^2}{4\sigma^2 + R^2}\ e^{-\frac{2r^2}{4\sigma^2 + R^2}}\ , \tag{4}$$

$$g_{Disk>}(r, R, \sigma) = \Phi\left(\frac{c_2 - 1}{c_1} + c_1\right)\ , \tag{5}$$

$$c_1 = \frac{2}{3}\,\sigma\,\frac{\sqrt{\sigma^2 + x^2 + y^2}}{2\sigma^2 + x^2 + y^2}\ ,\quad \text{and}\quad c_2 = \left(\frac{R^2}{2\sigma^2 + x^2 + y^2}\right)^{1/3}\ . \tag{6}$$

Fig. 2 shows 1D cross-sections (for different ratios R/σ) of the exact Gaussian smoothed cylinder g_{Disk} (numerically integrated), the two approximations $g_{Disk<}$ and $g_{Disk>}$, and our new model $g_{Cylinder}$. It can be seen that our model approximates the exact curve very well (see the *positive* axis). In addition, we include in our model the intensity levels a_0 (surrounding tissue) and a_1 (vessel) as well as a 3D rigid transform $\mathcal{R}$ with rotation parameters $\boldsymbol{\alpha} = (\alpha, \beta, \gamma)^T$ and translation parameters $\mathbf{t} = (x_0, y_0, z_0)^T$. This results in the parametric intensity model with a total of 10 parameters $\mathbf{p} = (R, a_0, a_1, \sigma, \alpha, \beta, \gamma, x_0, y_0, z_0)$:

$$g_{M,Cylinder}(\mathbf{x}, \mathbf{p}) = a_0 + (a_1 - a_0)\ g_{Cylinder}(\mathcal{R}(\mathbf{x}, \boldsymbol{\alpha}, \mathbf{t}), R, \sigma) \tag{7}$$

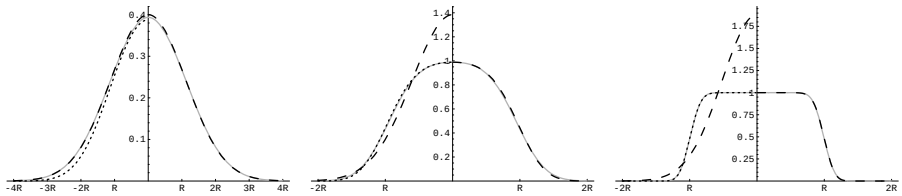

Fig. 2. For different ratios of $R/\sigma = 1.0; 3.0; 8.0$ (from left to right), the exact curve g_{Disk} of a 1D cross-section of a Gaussian smoothed disk is given (grey curve) as well as the approximations $g_{Disk<}$ and $g_{Disk>}$ (dashed resp. dotted curve for the *negative* axis) and the new model $g_{Cylinder}$ (dashed curve for the *positive* axis).

2.2 Optimal Values T_Φ and σ_Φ for the Blending Function

In order to determine optimal values T_Φ and σ_Φ for the blending function used in (3), we computed the approximation errors of the approximations $g_{Disk<}$ and $g_{Disk>}$ for different values of $\sigma = 0.38, 0.385, \ldots, 0.8$ and fixed radius $R = 1$ (note, we can fix R as only the ratio R/σ is important). The approximation errors were numerically integrated in 2D over one quadrant of the smoothed disk (using Mathematica). From the results (see Fig. 3 left and middle) we found that the approximation errors intersect at $\sigma/R = 0.555 \pm 0.005$ in the L1-norm and at $\sigma/R = 0.605 \pm 0.005$ in the L2-norm. We here chose the mean of both intersection points as threshold, i.e. $T_\Phi = 1/0.58 \approx 1.72$. It is worth mentioning that this value for T_Φ is much better than $T_\Phi = 1$ originally proposed in [1]. For σ_Φ we chose a value of 0.1. From further experiments (not shown here) it turns out that these settings give relatively small approximation errors in both norms. It nicely turns out (see Fig. 3 left and middle) that our model not only combines the more accurate parts of both approximations but also has a lower error in the critical region close to T_Φ, where both approximations have their largest errors.

2.3 Analysis for Thin Structures

For thin cylinders, i.e. $R/\sigma < T_\Phi$, our model $g_{Cylinder}$ is basically the same as the approximation $g_{Disk<}$, which has the following remarkable property for some factor f with $0 < f \leq f_{max} = \sqrt{1 + 4\sigma^2/R^2}$:

$$a\, g_{Disk<}(r, R, \sigma) = \frac{a}{f^2}\, g_{Disk<}\left(r,\ R' = fR,\ \sigma' = \frac{1}{2}\sqrt{4\sigma^2 + R^2\,(1 - f^2)}\right) \quad (8)$$

where a represents the contrast $a_1 - a_0$ of our model $g_{M,Cylinder}$ and $a' = a/f^2$. This means that this function is identical for different values of f, i.e. different settings of $R'(f)$, $\sigma'(f)$, and $a'(f)$ generate the same intensity structure. This relation is illustrated for one example in Fig. 3 (right). As a consequence, based on this approximation it is *not* possible to unambiguously estimate R, σ, and a from intensities representing a thin smoothed cylinder. In order to uniquely estimate the parameters we need additional information, i.e. a priori knowledge of one of the three parameters. With this information and the ambiguous estimates we are able to compute f and subsequently the remaining two parameters.

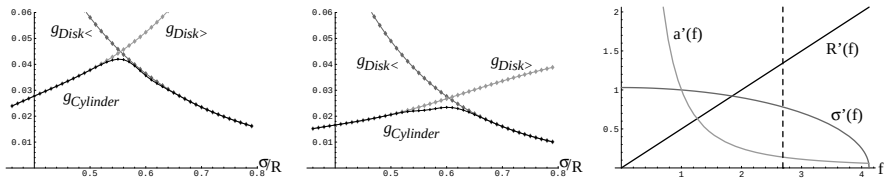

Fig. 3. For different values of $\sigma = 0.38, 0.385, \ldots, 0.8$ and radius $R = 1$, the errors of the approximations $g_{Disk<}$ and $g_{Disk>}$ (dark resp. light gray) as well as the error of the new model $g_{Cylinder}$ (black) are shown for the L1-norm (left) and L2-norm (middle). The right diagram shows $R'(f)$, $\sigma'(f)$, and $a'(f)$ for a varying factor f between 0 and f_{max} (for fixed $R = 0.5$, $\sigma = 1$, $a = 1$). The vertical dashed line indicates the ratio $f = R/\sigma = T_\Phi$, i.e. only the left part of the diagram is relevant for $g_{Disk<}$.

Obviously, it is unlikely that we have a priori knowledge about the radius of the vessel as the estimation of the radius is our primary task. On the other hand, even relatively accurate information about the smoothing parameter σ will not help us much as can be seen from (8) and also Fig. 3 (right): $\sigma'(f)$ is not changing much in the relevant range of f. Therefore, a small deviation in σ can result in a large deviation of f and thus gives an unreliable estimate for R. Fortunately, the opposite is the case for the contrast $a'(f)$. For given estimates $\hat{R}$ and $\hat{a}$ as well as a priori knowledge about a, we can compute $f = \sqrt{a/\hat{a}}$ and $R = \hat{R}/f = \hat{R}\sqrt{\hat{a}/a}$. For example, for an uncertainty of $\pm 10\%$ in the true contrast a the computed radius is only affected by ca. $\pm 5\%$, and for an uncertainty of -30% to $+56\%$ the computed radius is affected by less than 20%. Note, this consideration only affects thin vessels with a ratio $R/\sigma < T_\Phi = 1.72$, i.e. for typical values of $\sigma \approx 1$ voxel and thus a radius below 2 voxels, the error in estimating the radius is below 0.2 voxels even for a large uncertainty of -30% to $+56\%$.

We propose two strategies for determining a. In case we are segmenting a vessel with varying radius along the vessel, we can use the estimate of the contrast in parts of the vessel where $R/\sigma > T_\Phi$ (here the estimates of the parameters are unique) for the other parts as well. In case of a thin vessel without thicker parts we could additionally segment a larger close-by vessel for estimating the contrast, assuming that the contrast is similar in this region of the image.

Standard approaches for vessel segmentation based on a Gaussian function (e.g., [8],[7],[5]) only estimate two parameters: the image contrast a_g and a standard deviation σ_g. Assuming that the image intensities are generated by a Gaussian smoothed cylinder based on $g_{Disk<}$, we can write $a_g = 2aR^2/(4\sigma^2 + R^2)$ and $\sigma_g = \sqrt{4\sigma^2 + R^2}/2$, see (4). Often, the radius of the vessel is defined by the estimated standard deviation σ_g, which implies that $\sigma = R\sqrt{3}/2$ holds. However, this is generally not the case and therefore leads to inaccurate estimates of R.

3 Incremental Vessel Segmentation and Quantification

To segment a vessel we utilize an incremental process which starts from a given point of the vessel and proceeds along the vessel. In each increment, the parameters of the cylinder segment are determined by fitting the cylindrical model in (7) to the image intensities $g(\mathbf{x})$ within a region-of-interest (ROI), thus minimizing

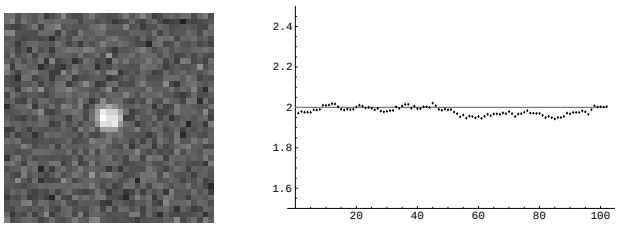

Fig. 4. Estimated radius R for 102 segments of a smoothed straight 3D cylinder with settings $R = 2$, $\sigma = 1$, $a_0 = 50$, and $a_1 = 150$ as well as added Gaussian noise ($\sigma_n = 10$). In addition, one 2D cross-section of the 3D synthetic data is shown.

$$\sum_{\mathbf{x} \in \mathrm{ROI}} \left(g_{M,Cylinder}\left(\mathbf{x}, \mathbf{p}\right) - g\left(\mathbf{x}\right) \right)^2 \tag{9}$$

For the minimization we apply the method of Levenberg-Marquardt, incorporating 1st order partial derivatives of the cylindrical model w.r.t. the model parameters. The partial derivatives can be derived analytically. The length of the cylinder segment is defined by the ROI size (in our case typically 9-21 voxels). Initial parameters for the fitting process are determined from the estimated parameters of the previous segment using a linear Kalman filter, thus the incremental scheme adjusts for varying thickness and changing direction.

4 Experimental Results

4.1 3D Synthetic Data

In total we have generated 388 synthetic 3D images of straight and curved tubular structures using Gaussian smoothed discrete cylinders and spirals (with different parameter settings, e.g., for the cylinders we used radii of $R = 1, \ldots, 9$ voxels, smoothing values of $\sigma = 0.5, 0.75, \ldots, 2$ voxels, and a contrast of 100 grey levels). We also added Gaussian noise ($\sigma_n = 0, 1, 3, 5, 10, 20$ grey levels). From the experiments we found that the approach is quite robust against noise and produces accurate results in estimating the radius as well as the other model parameters (i.e. contrast and image smoothing as well as 3D position and orientation). As an example, Fig. 4 shows the estimated radius for 102 segments of a relatively thin smoothed cylinder. The correct radius could be estimated quite accurately within ± 0.06 voxels along the whole cylinder. Fig. 5 (right) shows the differences of the estimated radius to the true radius of smoothed cylinders for a range of different radii (for $\sigma = 1$ and $\sigma_n = 10$). It can be seen that the error in the estimated radius is in all cases well below 0.1 voxels. As a comparison we also applied a standard approach based on a 3D Gaussian line. To cope with the general limitations of the Gaussian line approach (see Sect. 2.3), we additionally calibrated the estimated radius (assuming an image smoothing of $\sigma = 1$, see [5] for details). It can be seen that the new approach yields a significantly more accurate result in comparison to both the uncalibrated and calibrated Gaussian line approach (Fig. 5 left and middle). Fig. 6 shows segmentation results of our

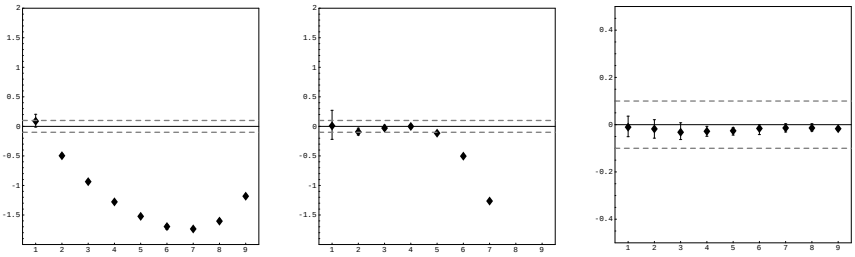

Fig. 5. Differences of the estimated radius (mean over ca. 99 segments) and the true radius for a synthetic straight cylinder with different radii $R = 1, \ldots, 9$ for the uncalibrated (left) and calibrated Gaussian line model (middle), as well as for the new cylindrical model (right). The dashed lines highlight the interval from -0.1 to 0.1 voxels.

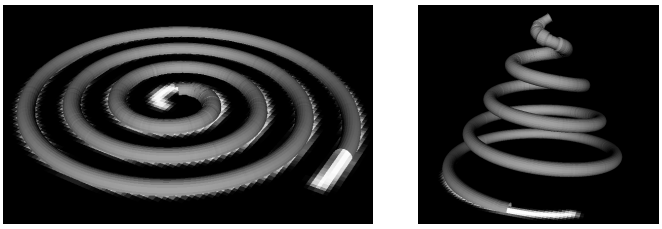

Fig. 6. Segmentation results of applying the cylindrical model to 3D synthetic data of a spiral (left) and a screw-like spiral (right). For visualization we used 3D Slicer [4].

new approach for a spiral and a screw-like spiral (for a radius of $R = 2$ voxels). It turns out that our new approach accurately segments curved structures of varying curvature, i.e. the estimated radius is within ± 0.1 voxels to the true radius for nearly all parts of the spirals. Larger errors only occur for the last part of the innermost winding, where the curvature is relatively large.

4.2 3D Medical Images

With our approach both position and shape information (radius) are estimated from 3D images. Fig. 7 shows segmentation results of applying the new cylindrical model to 3D MRA images of the human pelvis and heart. Note that for the segmentation of the vessel trees we used starting points at each bifurcation. It can be seen that arteries of quite different sizes and high curvatures are successfully segmented. As a typical example, the computation time for segmenting an artery of the pelvis (see Fig. 7 left, main artery in left branch including the upper part) using a radius of the ROI of 10 voxels is just under 4min for a total of 760 segments (on a AMD Athlon PC with 1.7GHz, running Linux).

5 Discussion

The new 3D cylindrical intensity model yields accurate and robust segmentation results comprising both position and thickness information. The model allows to accurately segment 3D vessels of a large spectrum of sizes, i.e. from very thin vessels (e.g., a radius of only 1 voxel) up to relatively large arteries (e.g., a radius

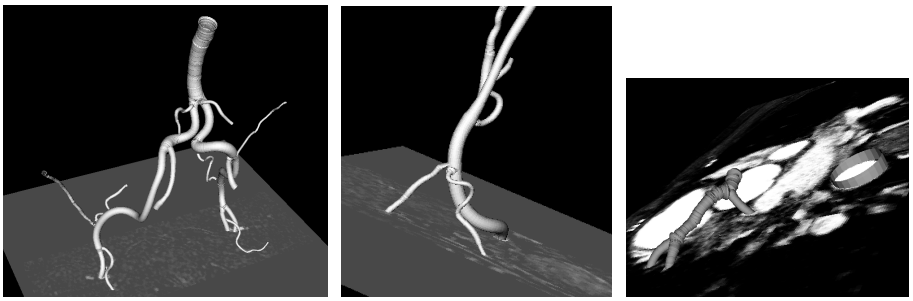

Fig. 7. Segmentation results of applying the new cylindrical model to arteries of the pelvis (left and middle) as well as to coronary arteries and the aorta (right).

of 14 voxels for the aorta). Also, we pointed out general limitations in the case of thin structures and disadvantages of approaches based on a Gaussian function.

6 Acknowledgement

The MRA images are courtesy of Dr. med. T. Maier and Dr. C. Lienerth, Gemeinschaftspraxis Radiologie, Frankfurt/Main, Germany, as well as Prof. Dr. T. Berlage and R. Schwarz from the Fraunhofer Institute of Applied Information Technology (FIT), Sankt Augustin, Germany.

References

1. M. Abramowitz and I. Stegun, *Pocketbook of Mathematical Functions*, Verlag Harri Deutsch, 1984
2. E. Bullitt, S. Aylward, K. Smith, S. Mukherji, M.Jiroutek, K. Muller, "Symbolic Description of Intracerebral Vessels Segmented from MRA and Evaluation by Comparison with X-Ray Angiograms", *Medical Image Analysis*, 5, 2001, 157-169.
3. A. F. Frangi, W. J. Niessen, R. M. Hoogeveen, *et al.*, "Model-Based Quantitation of 3D Magnetic Resonance Angiographic Images", *T-MI*, 18:10, 1999, 946-956
4. D.T. Gering, A. Nabavi, R. Kikinis, *et al.*, "An integrated Visualization System for Surgical Planning and Guidance using Image Fusion and Interventional Imaging", *Proc. MICCAI'99*, 1999, 808-819
5. R.H. Gong, S. Wörz, and K. Rohr, "Segmentation of Coronary Arteries of the Human Heart from 3D Medical Images", *Proc. BVM'03*, 2003, 66-70
6. Th.M. Koller, G. Gerig, G. Szkely, and D. Dettwiler, "Multiscale Detection of Curvilinear Structures in 2D and 3D Image Data", *Proc. ICCV'95*, 1995, 864-869
7. K. Krissian, G. Malandain, N. Ayache, R. Vaillant, and Y. Trousset, "Model Based Detection of Tubular Structures in 3D Images", *CVIU*, 80:2, 2000, 130-171
8. H.J. Noordmans, A.W.M. Smeulders, "High accuracy tracking of 2D/3D curved line structures by consecutive cross-section matching", *Pattern Recogn. Letters*, 19:1, 1998, 97-111
9. J.M. Reinhardt, N.D. D'Souza, and E.A. Hoffman, "Accurate Measurement of Intrathoracic Airways", *IEEE Trans. on Medical Imaging*, 16:6, 1997, 820-827
10. D. Rueckert, P. Burger, S.M. Forbat, R.D. Mohiaddin, G.Z. Yang, "Automatic Tracking of the Aorta in Cardiovascular MR Images Using Deformable Models", *IEEE Trans. on Medical Imaging*, 16:5, 1997, 581-590